www.czasopisma.pan.pl PAN www.journals.pan.pl

Opto-Electronics Review 25 (2017) 188–197

Contents lists available at ScienceDirect

Opto-Electronics Review

journal homepage: http://www.journals.elsevier.com/opto-electronics review

Topological insulators based on the semi-metallic HgCdTe

G. Tomaka, J. Grendysa, M. Marchewka, P. Śliż*, C.R. Becker, A. Stadler, E.M. Sheregii

Centre for Microelectronics and Nanotechnology, University of Rzeszow, ul. Pigonia 1, 35-959 Rzeszow, Poland

ARTICLE INFO

Article history:
Received 16 November 2016
Accepted 20 December 2016
Available online 12 July 2017

Keywords:
MCT solid solutions
Topologically protected surface states
Magneto-transport

ABSTRACT

The review of peculiarity of growth and experimental results of the magneto-transport measurements (longitudinal magneto-resistance R_{xx} and the Hall resistance R_{xy}) over a wide interval of temperatures for several samples of $Hg_{1-x}Cd_xTe$ ($x \approx 0.13$–0.15) grown by MBE is presented in this paper. An amazing temperature stability of the SdH-oscillation period and amplitude is observed in the entire temperature interval of measurements up to 50 K. Moreover, the quantum Hall effect (QHE) behaviour of the Hall resistance was shown in the same temperature interval. These peculiarities of the R_{xx} and R_{xy} for strained thin layers are interpreted using quantum Hall conductivity (QHC) on topologically protected surface states (TPSS). In the case of not strained layers it is assumed that the QHC on the TPSS contributes also to the conductance of the bulk samples. The experimental results on magneto-transport (QHC and SdH) obtained for the strained 100 nm thickness $Hg_{1-x}Cd_xTe$ layer are interpreted on the basis of the 8×8 **kp** model and an advantage of the $Hg_{1-x}Cd_xTe$ as topological insulators is shown. This article is an expanded version of the scientific reports presented at the International Conference on Semiconductor Nanostructures for Optoelectronics and Biosensors 2016 ICSeNOB2016, May 22–25, 2016, Rzeszow, Poland.

1. Introduction

Mercury Cadmium Telluride Alloys (MCT) are still main material for infrared devises [1] on the one hand but semimetal MCT is natural analogue of graphene in 3D on the other hand [2,3]. In another words, semimetal MCT is a 3D topological Dirac semimetal.

One of the obvious properties of semiconductors is their strong dependence on external conditions such as temperature, illumination, or pressure. Topological insulators (TI) discovered during the last decade have augmented our knowledge in this matter. TI is a new class of quantum matter with conducting surface states, topologically protected against time-reversal-invariant perturbations and an insulating bulk. The physics of TI links the structures of d dimensions with their boundaries in d-1 dimensions: a TI is a state of quantum matter that behaves as an insulator in its interior and as a metal on its boundaries [3].

This topic review paper describes experimental results obtained for bulk $Hg_{1-x}Cd_xTe$ samples with $x \approx 0.13$–0.16 corresponding to a semi-metallic type of band-structure, i.e. the Γ_8 band is higher than Γ_6 (in normal semiconductors as CdTe it is contrary: the Γ_6 band is above the Γ_8 bands and play role of the conduction band but Γ_8 bands are valence bands – bands of light and heavy holes), however, it is close to the critical point at which the Γ_6 and Γ_8 bands cross, that should occur in the temperature region from 0.4 to 150 K depending on the x value. Chapter III presents the experimental details: the samples grown by MBE technology, the magneto-transport experiment procedure, and experimental data including the SdH oscillations, the QHE behaviour of the Hall resistance observed in a wide temperature region for the samples with a different level of doping including comparably thick layers. In Chapter IV the origin of the Quantum Hall Conductance behaviour of the Hall resistance for thin strained MCT layers is discussed and for thin not strained layers and comparatively thick ones. Finally, in Chapter V are summaries of these findings and conclusions.

2. Topologically protected surface states (TPSS)

The first topological insulators which were observed via the quantum spin Hall effect concern a two-dimension electron gas (2DEG) with a spin structure on a 1D edge. They were discussed theoretically [4,5], predicted to occur in HgTe quantum wells [6], and then experimentally verified by König et al. [7]. Thereafter, Liang Fu et al. [8] proposed the 3D version of topological insulators, predicted to occur in Bi-Sb alloys by Fu and Kane [9], and experimentally detected with angle-resolved photoemission spectroscopy ARPES by Hsieh et al. [10].

Subsequently, the quantum Hall effect (QHE) in the surface layer with states caused by crossing of bands at surface – Topologically

* Corresponding author.
E-mail address: slizpawel@gmail.com (P. Śliż).

http://dx.doi.org/10.1016/j.opelre.2017.06.006
1230-3402/

Protected Surface States (TPSS) – was observed via transport experiments in strained bulk mercury telluride (HgTe) [11]. As predicted by Bernevig et al. [6], TPSS occur at the surface of HgTe as massless Dirac points (Dirac cones with a linear dependence of the electron energy on momentum in terms of the band structure) because of the Γ_6 and Γ_8 band crossing. Generally, it is caused by strong a spin-orbital interaction in these materials which lifts the Γ_8 band above the Γ_6 band in the bulk part of the sample [12].

This kind of TPSS is characterized by a Z_2 topological invariant, requiring gapless electronic states to exist on the boundary of the sample, which is a strong topological insulator and is robust in the presence of disorder [6,13,14]. Such strong topological insulators have surface states, with the Fermi surface enclosing an odd number of Dirac points and being associated with the Berry phase of Ref. [15]. This defines a topological metal surface phase which is predicted to have novel electronic properties [16–18].

There is some similarity with the half-Heusler alloys. For example, PtMnBi show semi-metallic properties in the α phase, and the effects of the spin-orbit interaction shifts of the valence bands and the indirect semiconducting gap with respect to the spin polarized results [19,20]. Also BiSb alloys, Bi_2Se_3, Bi_2Te_3 and Sb_2Te_3 crystals show the 3D TI properties [21–24]. The next class of bulk topological insulators discovered during the last decade includes $TlSbSe_2$, $TlSbTe_2$, $TlBiSe_2$ and $TlBiTe_2$ [25,26], as well as septuple-layer topological insulators [27].

Recently, well-developed TPSS were reported to occur in the QHE of $BiSbTeSe_2$, an intrinsic TI bulk material, 120 and 160 nm thick [28]. In addition, the dominate contribution of the surface metallic conductivity in the total sample resistance of BiSbTeSe above 120 K, was noticed. Thus, a new feature of the electron transport properties of semiconductors with a strong spin-orbital interaction could take place: the surface metallic conductance. The same, as will be shown below, can be said of mercury cadmium telluride solid solutions – arguably the best material for infrared devices [29–31]. The QHE according to Brüne et al. [11] (similar results were presented later in Ref. [32]) was displayed for comparably thin (70 nm) strained samples. It is interesting to check the same experiment for thin strained layers of semimetal alloys of HgCdTe, as well as for no strained layers of these alloys.

3. MBE growth

MBE is the most advanced technology for obtaining semiconductor layers widely used for synthesis of the layers of II–VI compounds [33–35]. The $Hg_{1-x}Cd_xTe$ samples were grown in a Riber Compact 21 molecular beam epitaxial (MBE) system. The CdTe and Te fluxes were chosen and subsequently adjusted in order to grow the $Hg_{1-x}Cd_xTe$ layers with a zero gap at approximately 4–50 K. Several conditions should be fulfilled during the growth process of the $Hg_{1-x}Cd_xTe$ layer with $0 < x < 0.16$ of high quality – with surface close to ideal and low density of defects (hillocks) [35].

First, the substrate temperature should be controlled with an accuracy not worthy than ±0.5 °C because of its strong influence on composition. The substrate temperature determination needs specific calibration due to lack of physical contact for thermocouple with a molybdenum substrate holder. Therefore, this thermocouple is calibrated by using the melting point of In, Sn and PbSn on holder.

Second, the determination and stabilization of the beam equivalent pressure (BEP) of sources (fluxes in others words) is principally important at MBE growth for each compound. In case of the $Hg_{1-x}Cd_xTe$ layer growth additional factor is essential: stabilization of the Hg-flux is difficult and long – for 2 h long. The composition is determined by the Cd/Te flux ratio whereas, the flux ratio Hg/Te is important for quality of received layers. Stabilization of these two ratio at the growth is crucial: deviation of BEP in the framework of 10^{-8} Torr able to change considerably the composition in the case of the Cd/Te ratio, as well as to increase the hillock density, electron concentration and decrease the electron mobility, in the case of the Hg/Te ratio.

Two types of substrates were used to perform the experiment: i) (001) oriented GaAs substrates were applied with the MBE grown CdTe buffer that produced ~0.3% mismatch with the next thin MBE grown $Hg_{1-x}Cd_xTe$ layer; ii) (112)*B* orientated CdZnTe substrates were employed and the $Hg_{1-x}Cd_xTe$ was grown directly on the CdZnTe(112)B substrate surface which has a lattice constant practically (with an uncertainty of 0.01%) equal to that of bulk $Hg_{1-x}Cd_xTe$ ($x \approx 0.13$). Consequently, three types of samples were grown and measured, namely: type A – $Hg_{1-x}Cd_xTe$ thin strained layers on the GaAs/CdTe substrates (about 100 nm thick); type AB – $Hg_{1-x}Cd_xTe$ thin not strained layers on the CdZnTe(112)B substrates (about 100 nm thick); type B – $Hg_{1-x}Cd_xTe$ thick not strained layers on the CdZnTe(112)B substrates (samples B4, B6-B9 are about 1 μm thick, the sample B5 is above 2 μm thick). The $Hg_{1-x}Cd_xTe$ layers were substantially doped with iodine by means of a CdI_2 effusion cell for samples A9, AB9, B8 and B9 and by means of an In effusion cell for samples A4, AB4, B4, B5 and B6. SIMS measurements and the reflection maxima of E_1 and $E_1 + \Delta_1$ in the region of fundamental absorption of the $Hg_{1-x}Cd_xTe$ alloys [36] were used to confirm the composition, level of doping and thickness of the grown layers (see Table 1).

4. Magnetotransport measurements

2 The magneto-transport measurements were performed using a cryo-magnet system from ICEoxford, which is capable of voltage measurements in the temperature region from 0.25 to 290 K in magnetic fields up to 14 T. The direction of the magnetic field B was perpendicular to the plane of the investigated layer in the samples. Four-terminal longitudinal (R_{xx}) and Hall (R_{xy}) resistances were measured with standard lock-in techniques at a low-frequency (<20 Hz) and with an excitation current of 0.5–1.0 μA. Four measurements were made, i.e. for the two directions of the magnetic

Table 1
Parameters of the samples grown by MBE.

No.	Composition x, mol.	Substrate	Thickness, nm	Level of the iodine bulk doping 10^{17} cm^{-3}	Level of the indium bulk doping 10^{17} cm^{-3}
A4	0.155	GaAs/CdTe(001)	100		0.5
A9	0.135	GaAs/CdTe(001)	100	5.0	
AB4	0.155	CdZnTe(112)B	100		0.5
AB9	0.135	CdZnTe(112)B	100	5.0	
B4	0.155	CdZnTe(112)B	840		0.5
B5	0.135	CdZnTe(112)B	2480		0.8
B6	0.150	CdZnTe(112)B	1280		3.0
B8	0.145	CdZnTe(112)B	950	0.5	
B9	0.135	CdZnTe(112)B	1100	5.0	

Parameters of the resulting layers are shown in Table 1. Fifteen samples with different compositions ($x = 0.13–0.16$), thicknesses and levels of doping, were investigated.

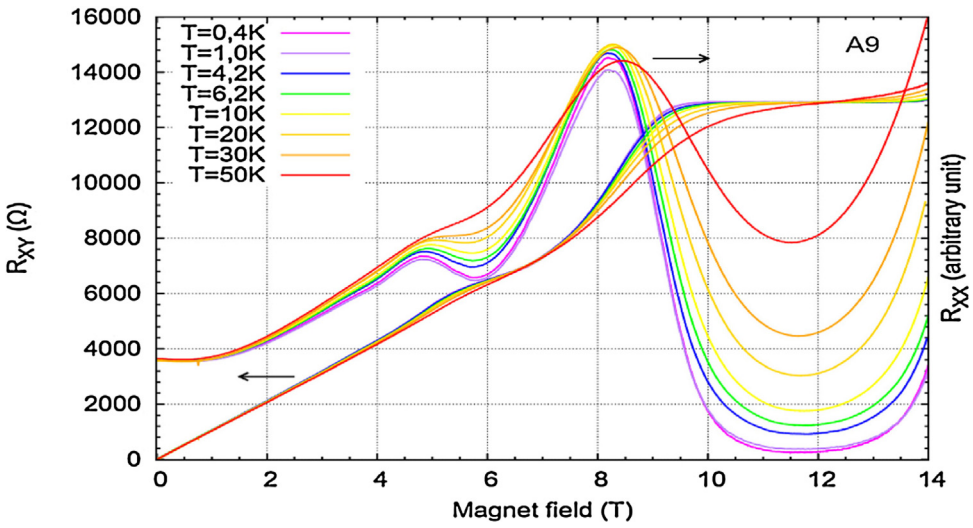

Fig. 1. Magneto-resistances, R_{xx} and R_{xy} vs magnetic field in the temperature region of 0.4–50 K for sample A9. Three plateaus are seen on the R_{xy} curves; the resistances in these plateaus in the temperature region of 0.4–20 K is equal to values $h/\nu e^2$ when $\nu = 2,4$ and 6.

field and for increasing and decreasing magnetic fields, with the subsequent averaging of each measurement of the longitudinal magneto-resistance and Hall resistance at a given temperature.

The results of the magnetotransport measurements obtained for sample A9 – strained thin layer on the GaAs/CdTe substrate – are presented in Fig. 1. The $R_{xx}(B)$ and $R_{xy}(B)$ curves are shown for different temperatures over a wide range from 0.4 K to 50 K. The welldefined quantized plateaus in R_{xy} with values $h/(2e^2) = 12.9$ kΩ, accompanied by vanishing R_{xx} is observed at 0.4 K.

It is seen pronounced plateaus in R_{xy} at values equal to about 6.5 kΩ as well as one less clear at about 4.3 kΩ The $R_{xx}(B)$ curves exhibit pronounced SdH-oscillations which positions of maxima strongly corresponds to stairs before plateaus on the $R_{xy}(B)$ curve. Described particularities on the $R_{xx}(B)$ and $R_{xy}(B)$ curves of sample A9 explicitly indicate on the Integer Quantum Hall Effect (IQHE) and Shubnikov-de Haas (SdH) oscillations characteristic for a 2D electron gas. The quantization in the integer multiples of $\sigma_0 = e^2/h$ is evident with the Landau filling factor ν equals 2, 4 and 6. It is necessary to underline that the $R_{xx}(B)$ and $R_{xy}(B)$ curves are reproducible up to 20 K and above this temperature the Integer Quantum Hall Conductivity (IQHC) is observed up to 50 K.

The same magneto-transport measurements are repeated for sample AB9 – no strained thin layer on the CdZnTe(112)B substrate. The remarkable temperature stability of the $R_{xx}(B)$ and $R_{xy}(B)$ curves characteristic for sample A9 is repeated for sample AB9 (see Fig. 2a).

Similarly, one can see the plateau-like features of the R_{xy} curve and corresponding SdH maxima on the $R_{xx}(B)$ curve, but the quantization in integer multiples of $\sigma_0 = e^2/h$ is not evident. The latter can be attributed to the availability of a parallel conductance channel from the sample interior that decreases the values of the R_{xy} resistance in the plateaus [37,38]. In order to more quantitatively estimate the surface contribution to the total conductance, we fit our data to a simple model used in Refs. [38,39], where the total conductance is the parallel sum of the bulk conductance of $Hg_{1-x}Cd_xTe$ ($x = 0.13$) and the 2D surface conductance. According to this scheme, the values of R_{xy} for the plateaus of QHE decrease proportionally due to the contribution of the bulk part of the sample. The calculation of the R_{xy} resistance (for the whole sample) assumed that the QHE values $R_{xx} = h/\nu e^2$ of the voltage are generated in the surface sheet, and the classic Hall Effect occurs in the bulk part of the sample. The results of calculation and experimental data obtained for the sample AB9 are compared in Fig. 2b. It can be seen that the results of simulation approximate very well the observed plateaus in the case of odd values of the filling factor: $\nu = 3, 5, 7$. Similar experimental data take place for sample AB4 also thin layer of semimetal $Hg_{1-x}Cd_xTe$ ($x = 0.155$) grown on the CdZnTe(112)B substrate.

Figs. 3–4 show the measurements for four samples from those listed in Table 1: B4, B5, B6 and B9 which are thick not strained layers. The $R_{xx}(B)$ and $R_{xy}(B)$ curves recorded for sample B9, are shown in Fig. 3a for different temperatures over a wide range from 0.4 to 50 K. It is noteworthy that the results are reproducible at different temperatures up to 50 K that seems unexpected for this thick sample (about 1 μm, see Table 1). Temperature increase beyond 50 K makes the plateaus less pronounced. The amazing temperature stability also concerns the positions of the observed SdH-oscillation maxima. These positions are reproducible up to 45 K and the amplitude of the SdH-maxima decreases slowly with increasing temperature above 50 K. The plateaus like features in R_{xy} in Figs. 3a and 4 are reminiscent of the IQHE but in the present case the values of the R_{xy} resistance in the plateaus for sample B9 are low, of the order of 10–20 Ω. From other hand, in case of sample B9 the ratio $R^{III}{}_{xy}(B)/R^{V}{}_{xy}(B) = 20.0\,\Omega/13.0\,\Omega = 1/3$: 1/5 and $R^{V}{}_{xy}(B)/R^{VII}{}_{xy}(B) = 13.0\,\Omega/11.0\,\Omega = 1/5{:}1/7$ where $R^{III}{}_{xy}$ is the value of resistance in the plateaus at 11.0–14.0 T, $R^{V}{}_{xy}(B)$ is the value of resistance in the plateaus at 7.0–8.5 T and $R_{xy}{}^{VII}(B)$ is the resistance at 5.5–6.5 T. Thus, these values of the resistance correspond to the magnitude for corresponding values of the filling factor of $\nu = 3$, 5 and 7, but they are smaller due to the parallel resistance in the sample. Similarly to the sample AB9, the calculation of the R_{xy} resistance (for the whole sample) assumed that the QHE values $R_{xy} = h/\nu e^2$ (ν is an integer) of the voltage are generated in the surface sheet, and the classic Hall Effect occurs in the bulk part of the sample. The results of the calculation are compared with the experimental curve for sample B9 in Fig. 3b. It can be seen that the results of simulation approximate satisfactorily the observed plateaus in the case of odd values of the filling factor: $\nu = 3, 5, 7$.

Similar curves were obtained for all samples of the B series. The results of the magneto-transport measurements obtained for samples B4, B5 and B6 are shown in Fig. 4 at approximately the same temperature (within an interval of 0.42–2.25 K). They exhibit the QHE behaviour similar to that observed for the sample B9, even though the plateaus values of the resistance are different due to their dependence on the resistance of the bulk part of the samples.

Moreover, the proportions between values of the R_{xy} resistance corresponding to odd values of the ν factor in different plateaus are retained. For sample B5 the plateaus in the $R_{xy}(B)$ curve are less

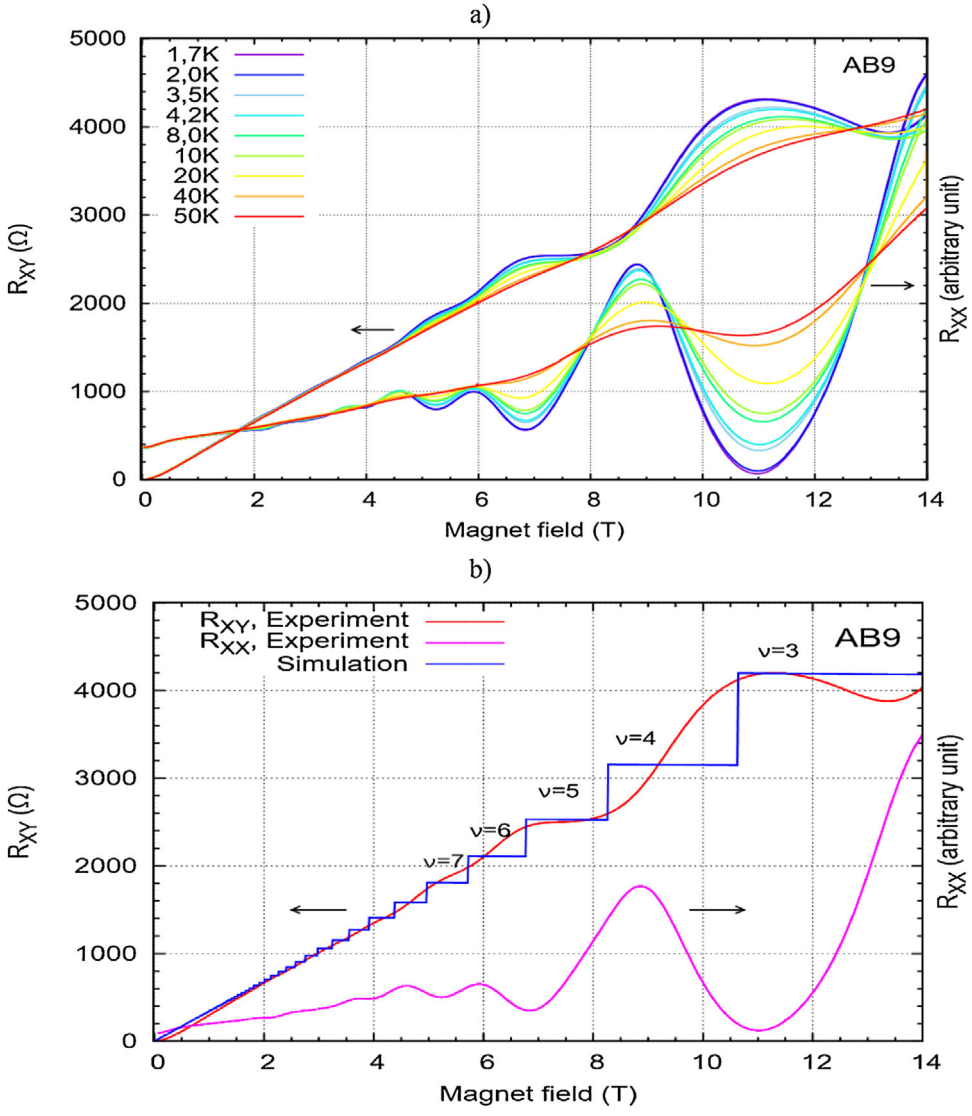

Fig. 2. a) Magneto-resistances, R_{xx} and R_{xy} vs magnetic field in the temperature region of 0.4–50 K for sample AB9; b) Calculations (blue line) of the R_{xy} resistance for the entire sample AB9 at 1.7 K performed according to a scheme of taking the parallel sum of the QHE values of the voltage generated in the surface sheet and a classic Hall voltage in the bulk part of sample AB9. It can be seen that the odd values of the filling factor $\nu = 3, 5, 7$ and 9 correspond to experimentally observed plateaus at temperature 1.7 K.

distinct. The results of calculating the $R_{xy}(B)$ resistance obtained in a similar way as for the samples AB9 and B9, are shown in Fig. 4 also. The stability of the R_{xy} and R_{xx} curves for samples B4 and B6 in the temperature interval of 0.4–45 K is similar to that of the sample B9. Other temperature behaviour is observed for sample B5: the plateaus and SdH oscillations disappeared after reaching 30 K.

It is interesting to note that in the case of 2DEG in the HgCdTe/HgTe/HgCdTe quantum well the resistance at the charge neutrality point was found to be temperature independent at low temperatures [40].

5. Electron transport on TPSS

5.1. General consideration

The model proposed for bulk HgTe [11] seems the most appropriate tool to explain the above results of magnetotransport measurements made for the $Hg_{1-x}Cd_xTe$ strained layer A9 (similar ones are for A4). The TPSS exist at the border of the sample surface layer with air, as well as at the border with the substrate whose 2D-layers with Dirac fermions contribute to the electron transport of the whole sample with the energy gap in the interior. Based on the studies made by cited above authors [11,30,37] and considering earlier works [41,42] we can understand the observed IQHC as the sum of a half integer QHC from the top surface and another half integer QHC from the bottom surface. In other words, the IQHC is quantized according to

$$\sigma_{xy}^{total} = \nu \frac{e^2}{h} = \sigma_{xy}^{top} + \sigma_{xy}^{bottom} = (\nu_t + \nu_b)\frac{e^2}{h} = (N_t + N_b + 1)\frac{e^2}{h} \quad (1)$$

with top (bottom) surface QHC

$$\sigma_{xy}^{top(bottom)} = \nu_{t(b)} \frac{e^2}{h} = \left(N_{t(b)} + \frac{1}{2}\right)\frac{e^2}{h} \quad (2)$$

where $\nu_{t(b)}$ and $N_{t(b)}$ are the Landau filling factor and Landau level index of top (bottom) surface corresponding to the QH state.

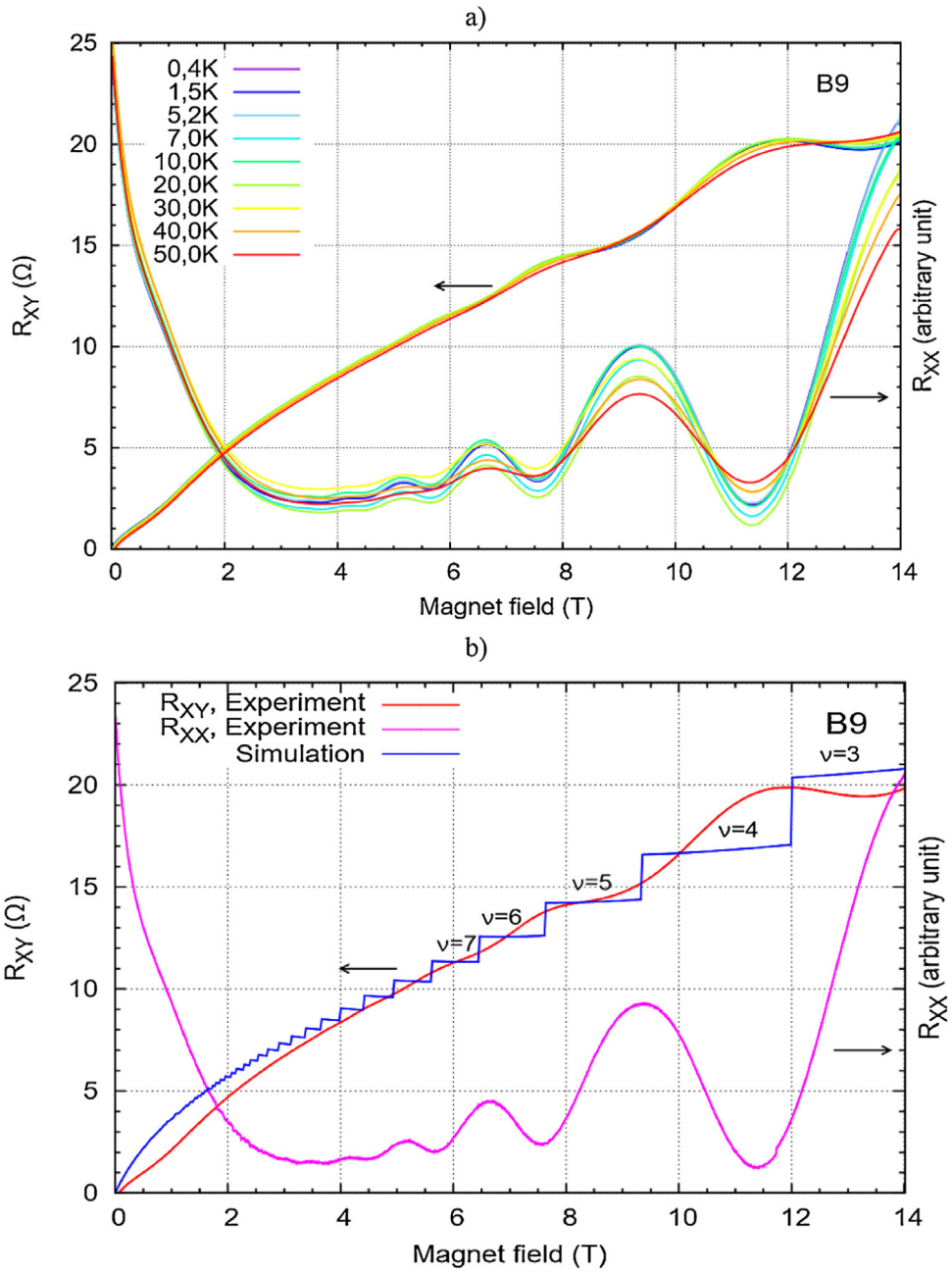

Fig. 3. a) Magneto-resistances, R_{xx} and R_{xy} vs. magnetic field in the temperature region of 0.4–50 K for sample B9; b) Calculations (blue line) of the R_{xy} resistance for the entire sample B9 at 4.2 K performed according to the same scheme as for sample AB9. It can be seen that the odd values of the filling factor $\nu = 3$, 5 and 7 correspond to experimentally observed plateaus.

When top and the bottom surface have the same filling factor, and both surfaces have the same density, i.e. $N_t = N_b$ then the resulting expression for the QHC, according to (1), is as follows:

$$\sigma_{xy} = (2N + 1)\frac{e^2}{h} \tag{3}$$

Hence, the filling factor ν can only have odd values.

In case of asymmetric conductivity along top and the bottom surface the expression (1) should be applied and the filling factor ν can be even or half-integer value if the conductivity along the bottom surface disappeared.

5.2. *Samples of A series*

The strong TI exists in the case of the sample A9: the energy gap of about 10 meV is formed in the sample interior due to the tension, and the TPSS are on surfaces due to the crossing of the Γ_8 and Γ_6 bands, similarly to a HgTe strained layer [11]. On the other hand, we should assume that the conditions of electron transport are different on the top and bottom surfaces because the first one is practically ideal (according to the AFM picture), but the bottom surface could be in a different situation at the interface with the CdTe buffer layer due to a mismatch. It means that the asymmetric conductivity along the top and bottom surfaces could be produced by the latter fact, namely – different density of the fermions.

As was shown in Chapter II the $R_{xy}(B)$ curves demonstrate the QHE with the Landau filling factor ν equals 2, 4 and 6 in the case

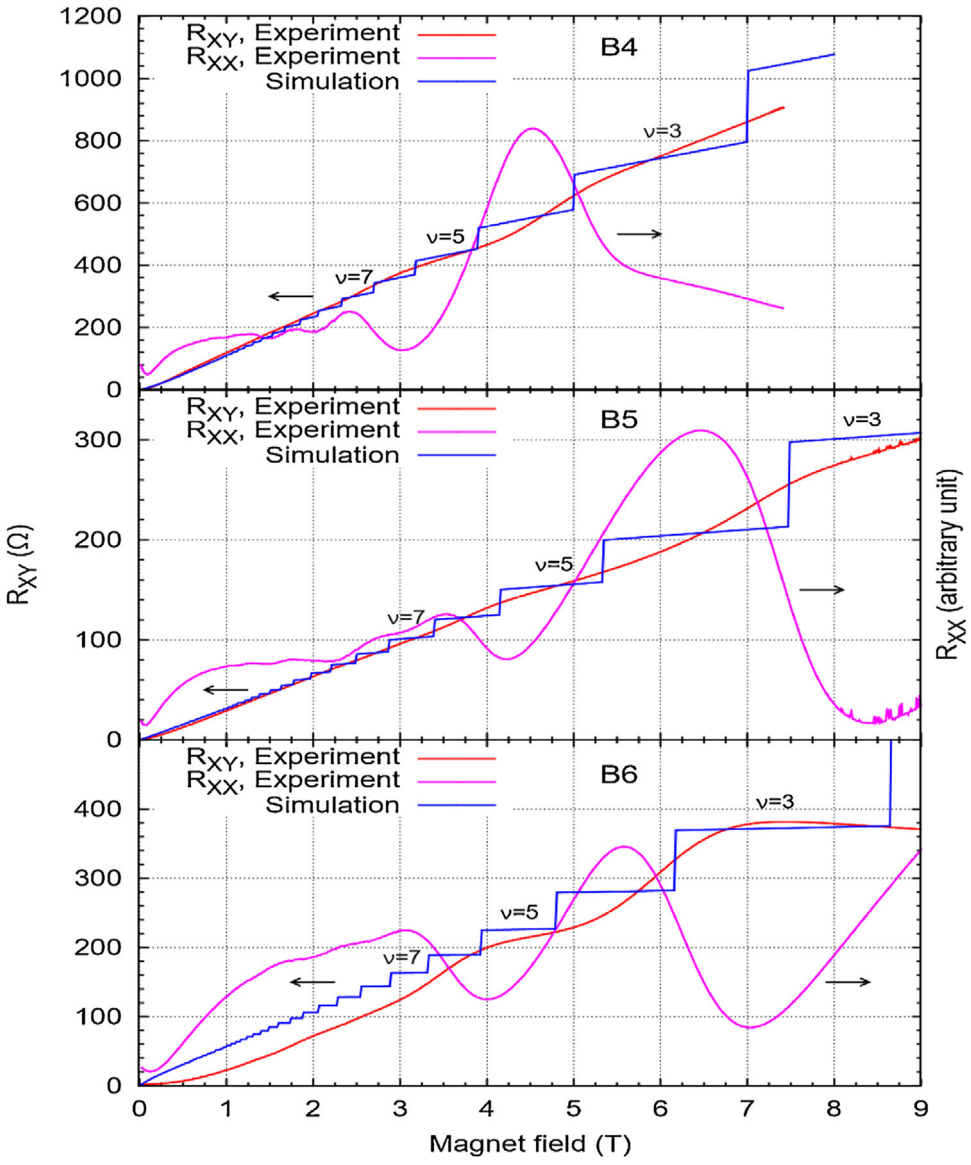

Fig. 4. Magneto-resistances, R_{xx} and R_{xy} vs. magnetic field in the temperature region of 0.4–2.3 K for samples B4, B5 and B6.

of sample A9. So, the filling factor is even, and, according to the expression (1) the next situation may be realized, for example: in case of $\nu = 2 - N_t = 0$ and $N_b = 1$, for $\nu = 4 - N_t = 1$ and $N_b = 2$ and for $\nu = 6 - N_t = 2$ and $N_b = 3$. The theoretical analyses of these results will be performed in Chapter V.

5.3. Samples of AB series

The sample AB9 was obtained by MBE growth on the CdZnTe(112)B substrate with practically ideal match. Thus, there are no strains, and there is no origin of the energy gap in the sample interior. On the other hand, it is difficult to refute that in semimetallic $Hg_{1-x}Cd_xTe$ ($x < 0.16$), between the nominally designated conduction and valence bands, a small gap can occur due to various reasons (finally, this gap may be generated by a magnetic field). So, it possible to assume that TPSS can exists in case of samples AB9 and AB4 on the background of a small energy gap or on the background of the heavy hole states [4,43] (without gap between of the $\Gamma_8^{1/2}$ and $\Gamma_8^{3/2}$ states, which they could be named as some resonance interface state, see more discussions below). This makes possible the same density of the Dirac fermions on top and bottom surfaces. In this case the IQHC according to Eq. (3) could be realized with odd values of the filling factor ν but the parallel classic Hall effect takes place in the interior of the sample without an energy gap. This assuming is confirmed by Fig. 2b where the simulation curve approximates very well the observed plateaus on the R_{xy} experimental curve for sample AB9 and odd values of the filling factor: $\nu = 3, 5, 7$. High temperature stability of the observed plateaus visible on the R_{xy} curves and of the SdH oscillations on the R_{xx} curves can be explained by this assuming the electron transport on the TPSS [or on the resonance interface state [43,44] (RIS)] dominates the electron transport in the whole sample AB9. This assuming concerns the sample AB4 also.

If the model of the electron transport applied to the sample AB9 is adequate, it becomes important to determine the thickness of a layer in which the Dirac fermions transport dominates. The experimental data obtained for the samples of B series could give an answer to this question.

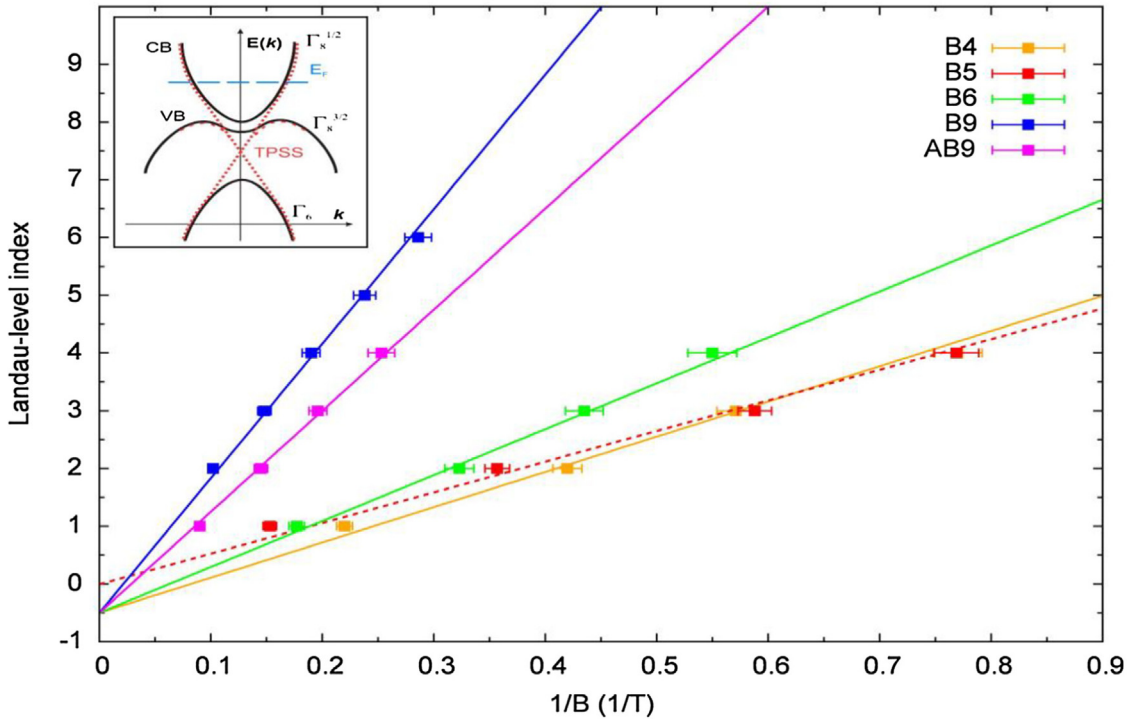

Fig. 5. Landau level index for the data of Figs. 2b, 3b and 4 plotted as a function of inverse magnetic field. The intercept of this plot for infinite magnetic field gives a value of −1/2 for samples AB9, B9, B4 and B6, which provides evidence that the observed IQHC can be well described by the two Dirac cones model. In the case of the B5 sample a spin splitted maxima of the SdH-oscillations are visible and the positions corresponded to the −N Landau index, are plotted what gives intercept "0". In the insert, the proposed energy band structure with TPSS is shown.

5.4. Samples of B series

It is appropriate to start with the sample B9 which can be considered as a thicker version (1100 nm thick) of the sample AB9. As was shown in Chapter II, for the sample B9, the plateaus at 11.0–14.0 T correspond to $\nu = 3$ and next one at 7.0–8.5 T—to $\nu = 5$, and another one at 5.5–6.5 T—to $\nu = 7$ (see Fig. 3b). Thus, the odd integer IQHC is observed as it has been described for the sample AB9, but the plateaus resistances are considerably less because of the substantial contribution from the classical Hall Effect in the sample bulk. High temperature stability of plateaus on the R_{xy} curves, as well as of the SdH oscillations on the R_{xx} curves shown in Fig. 3a in wide temperature range, allows advancing the hypothesis concerning a major role which the electron transport on the RIS (or on the TPSS) plays in the electron transport within the whole sample B9, as well.

As to the samples B4 and B6, it should be noted that experimental data confirm the hypothesis given above. The only exception is the sample B5 with the thickness of 2840 nm (Table 1).

5.5. Landau index as function on 1/B

The above mentioned interpretation of the experimental results concerning the Landau level structure of a Dirac system can be confirmed by plotting the Landau level index as a function of *1/B* [11,37,42]. That concerns mostly the samples of the series AB and B. Fig. 5 is created through taking the magnetic field values corresponding to the Hall plateaus with $\nu = 9, 7, 5, 3$ from the R_{xy} curve in Figs. 2b, 3b and 4 to plot the resulting N as a function of *1/B* according to Eq. (3). The intercept of these plots for infinite magnetic field gives in case of samples AB9, B9, B4 and B6 a value of −1/2, that provides additional evidence for describing the observed IQHC by the two Dirac cones model. For the sample B5 the intercept gives a 0 value that means the peculiarities visible on the R_{xx} curves can be attributed rather to the bulk part of the sample.

It is an unexpected result that the 2D-TPSS conductance (in case of thick samples B9, B4 and B6 we prefer to call: the electron transport on the RSI) contributes to the total conductance in these slab-shaped samples with parallel top and bottom surfaces which surround (together with the side walls) a thick (about 1 μm) semimetal bulk component (topologically it is the same as a sphere). Surprisingly the Dirac point in the surface layer can exist in conjunction with the (heavy hole) band in the bulk part of the sample (see inset in Fig. 5) without an energy gap (in case of samples of series AB and B) which usually takes place in TI. As was shown in Ref. [43], such TPSS states, designated as interface states, can couple to a heavy hole state and thus could be modified. Jie Ren *et al.* [44] illustrated the topological phase transition from bulk CdTe to HgTe upon alloying and the massless Dirac-Kane semimetal phase at the critical composition ($x < 0.16$) by computations based on a mixed-pseudopotential simulation confirmed by the ARPES experiment: a topological surface state (TSS) band connecting from the Γ_6 band to the upper Γ_8 band (above the Fermi level) takes place.

An alternative interpretation of above presented results on the AB and B series samples could be the possibility of a surface layer at interface layer-air produced due to increase of the mercury content at surface of the layer. That could form a narrow quantum well with 2DEG at interface what could generate observed IQHC. Probability of that is negligible due to whatever any increase in the Hg content at surface was registered by SIMS in samples investigated. On the other hand, if such quantum well could exists at surface, the QHE would show all integer values of the Landau filling factor not only odd values and the intercept of the resulting *N* plotting as a function of the *1/B* would give value 0 not −1/2 as it takes place for samples AB9, B9, B4 and B6 (see Fig. 5).

Another interesting feature is that the observed IQHC is more pronounced in samples B6 and B9 which have higher electron densities. Specific screening properties of Dirac systems [45–47] can originate this phenomenon.

Increase of temperature leads to increase in the contribution of interior of sample. At low temperatures (0.4–50 K) this contribution is less and the conductivity of a surface layer with TPSS (about of 3 nm thickness) dominates and leads to amazing temperature stability of electron transport. This unique fact can be explained in that the scattering on ionized impurities, parent at low temperatures in ordinary semiconductors, practically do not play a role in the electron transport on TPSS. As it was noticed in Chapter II this kind of TPSS is characterized by a Z_2 topological invariant, requiring gapless electronic states to exist as edge states on the boundary of the sample and is robust in the presence of disorder. That means the Dirac fermions form the Kramer's pairs each with different spin and cannot be scattered because different spin means opposite direction of moving and common momentum should be zero [5,13].

Increase of temperature above 50 K causes that the contribution of 3D bulk conductivity overcomes the 2D conductivity on TPSS and the plateaus disappear on the R_{xy} curves while the SdH oscillation maxima are shifted toward higher magnetic fields on the R_{xx} curves: electrons of interior of a layer with more high effective mass contributes into the SdH oscillations what leads to the shift of positions of SdH oscillations.

6. Advantages of semimetal MCT as topological insulator

The experimental results on magneto-transport (QHC and SdH) obtained for the strained 100 nm thickness $Hg_{1-x}Cd_xTe$ layer were interpreted on the basis of the 8×8 kp model [48]. The kp model used an eight band description of the band structure including all second-order terms representing the remote-band contributions with the first-order terms attributed to the $\Gamma_8^{3/2}$ – heavy hole, $\Gamma_8^{1/2}$ – light hole bands, and the $\Gamma_6^{1/2}$ – conduction band, as well $\Gamma_7^{1/2}$ – cleaved by the spin-orbital interaction. The available band-structure parameters used in the eight band description, are presented in Table 2. The detailed descriptions of the calculation and the results for the mixed $Hg_{1-x}Cd_xTe$ 3D TI for the different thickness of the layers and different tensile strain are presented in Ref. [48]. The calculations of the energy spectrum are provided in the framework of the envelope function approach where z – axis coincides with the growth direction of the 3D system. The finite difference method with the common central difference form is particularly employed in the discretization procedure.

The results of magneto-transport measurements are compared with the calculation of the Landau Level (LL's) energy obtained for A9 sample which was grown on GaAs/CdTe substrate (see Table 1).

Table 2
Band-structure parameters of the 8×8 kp model of the CdTe and HgTe applied proportionally to composition x to $Hg_{1-x}Cd_xTe$.

	HgTe	CdTe		HgTe	CdTe
E_g	−0.303 eV	1.606 eV	K	−0.4	−1.31
E_v	0	−0.570 eV	C	−3.83 eV	−4.06 eV
Δ	1.08 eV	0.91 eV	a	0	−0.7 eV
E_p	18.8 eV	18.8 eV	b	−1.5 eV	−1.17 eV
F	0	−0.09	d	−2.08 eV	−3.2 eV
γ_1	4.1	1.47	C_{11}	53.6 GPa	53.6 GPa
γ_2	0.5	−0.28	C_{12}	36.6 GPa	37.0 GPa
γ_3	1.3	0.03	C_{44}	21.2 GPa	19.9 GPa

The LL energy is presented in Fig. 7a. The even filling factor ν values of 2, 4 and 6 means that two independent surfaces should be taken into account in the fermion transport – on top and bottom of a sample. As it is shown in Fig. 7c and d to get the filling factor $\nu = 2$ it is necessary to have the Landau index $N_b = 1$ (bottom surface) and $N_t = 2$ for top surface. The LLs presented in Fig. 7 were calculated from above mentioned eight band kp model but the experimental data can also be fitted by the LL's fan energy obtained from graphene-like Hamiltonian. In order to obtain a good agreement with the graphene-like LL's energies and experimental curves of R_{xy} and R_{xx} the difference between the positions of the Dirac points for two surfaces should by equal about 40 meV. It is necessary to underline that the LL's fan calculated by the 8×8 kp model with band-structure parameters presented in Table 2, are in excellent agreement with that obtained using the graphene Hamiltonian as it is presented in Fig. 7a but then the Fermi level velocity is equal to about 0.95×10^6 m/s.

It is interesting to note that the same calculations performed for pure HgTe (x = 0) lead to the Fermi level velocity $v_F = 0.43 \times 10^6$ m/s what confirms the result obtained by authors of Ref. [11] ($hv_F = 280$ meV*nm). Using the relation $E_F = h\, k_F v_F$, it is possible to obtain from Fig. 7 the Fermi velocity for the electron at the TPSS. For the HgCdTe strained layers the velocity of the charges for the TPSS located on the right side of the structures – at the boundary with the vacuum (see Fig. 7c) – is two times higher than for the pure HgTe, and is equal $v_F = 0.9 \times 10^6$ m/s.

Such velocity allow to observe the quantized Hall conductance on TPSS even without external gate voltage and on the background of the bulk states. It is interesting to remark that the TPSS are visible in magneto-transport for the wide range of the gate voltage applied into the pure HgTe 3D 70-nm-thick sample due to their remarkable screening properties according to Ref. [47]. This hypotheses could

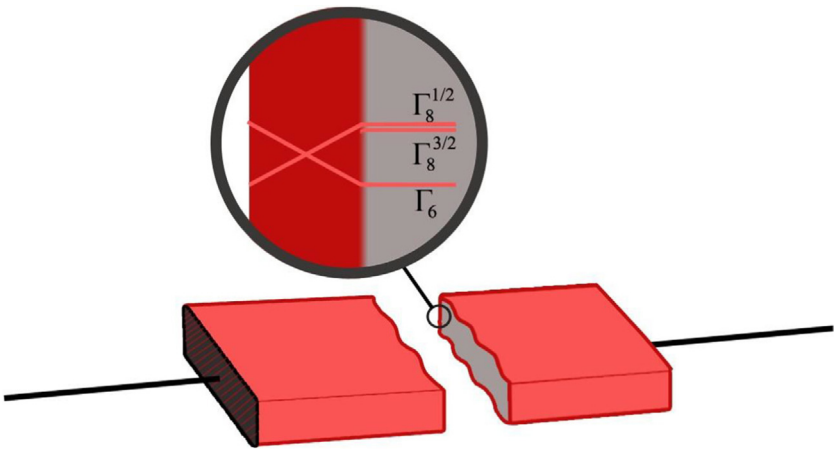

Fig. 6. Proposed conception of the electron transport in the semimetal bulk $Hg_{1-x}Cd_xTe$: the 2D-TPSS on parallel top and bottom surfaces (as well as on the side walls) form the metallic Berry phase (red colour) surround the bulk semimetal part (grey colour). As a result, metallic conductance on surfaces dominates the conductance of the entire sample.)

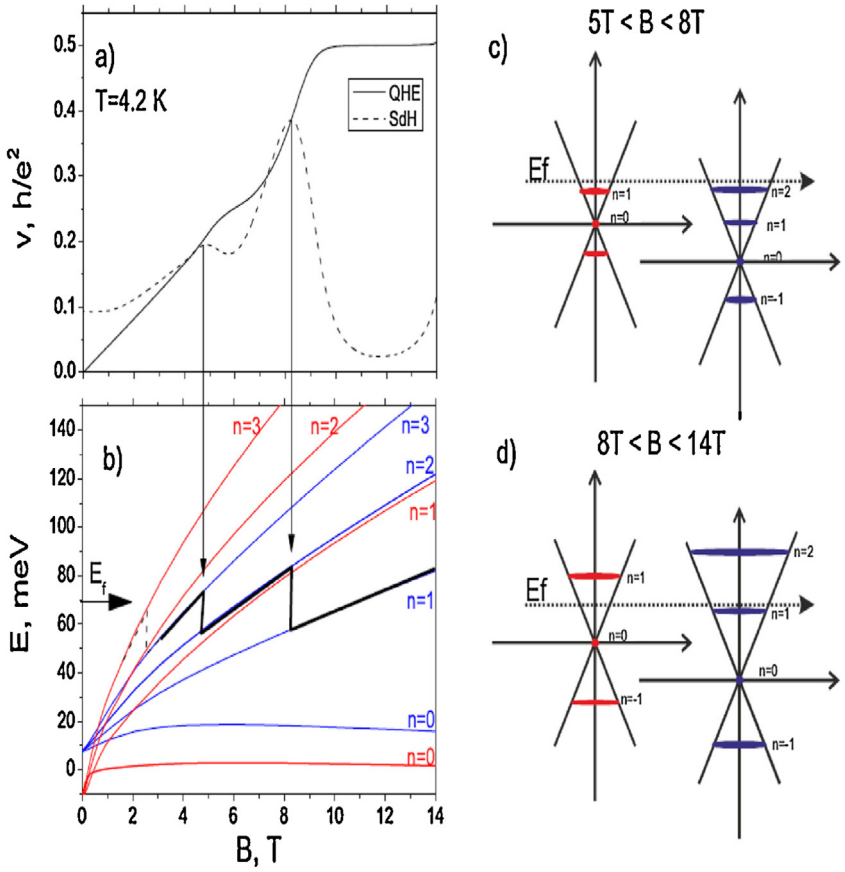

Fig. 7. a) The SdH oscillations and the IQHE for 4.2 K for 100 nm wide Hg0.865Cd0.135Te and b) the LL's fan calculated for two Dirac cones for two interfaces; c) and d) represent the LL's under the magnetic field region between 5 and 8T and 8 and 14 T, respectively.

be applied to our $Hg_{0.865}Cd_{0.135}Te$ sample also because high electron density. Besides, the high temperature stability of observed TPSS was shown in Ref. [2].

It is shown in Fig. 7 that the LL's fan calculated for TPSS for studied HgCdTe alloy using the 8×8 **kp** model corresponds to the one calculated by graphene Hamiltonian and characterized by $v_F \approx 0.95 \times 10^6$ m/s what is in excellent agreement with experimental IQHE- and SdH-curves. On the other hand, this value of the Fermi velocity is two times greater as for the strained HgTe TI [11] and for others kind of TI – approximately 5×10^5 ms^{-1}, for Bi_2Se_3 [20], or 3.4×10^5 ms^{-1} for the same compound according to Ref. [21].

So, the strained 3D $Hg_{0.865}$ $Cd_{0.135}Te$ is Topological Insulator with high value of the Fermi velocity (approximately the same as for graphene) what means significant advantages for future applications. Besides, the more high value of the energy gap inside sample as in case of strained HgTe, as well as a higher position of the Dirac points on the energy scale (all these advantages follow from significantly lower value of the electron momentum on the Fermi level in comparison with pure HgTe: the energy dispersion is closer to linearity in the wider range of the momentum) leads to an increase in the attractiveness of the Topological Insulator based on semimetal HgCdTe alloy for future applications: as massless Weyl fermions for example with addition of non-compensated spins of Mn [49].

7. Conclusions

Presented above review of results concerning the semi-metal MCT enable us to formulate some new properties of this class of material.

First, a quantized Hall conductance in the 3D $Hg_{1-x}Cd_xTe$ samples ($x < 0.16$) with the thickness from 100 to 1280 nm and with different levels of *n* type doping, using either iodine or indium as dopants, was observed [2] over a wide temperature region from 0.4 to 50 K.

Second, the experimental results lead to the hypothesis that quantum Hall conductance on the 2D-TPSS (or on the RSI) contributes to conductance of entire samples of semi-metallic MCT.

Third, a simple model with two Dirac cones satisfactorily explains the most salient features of the transport measurement of MBE grown and comparatively thick samples (up to 1280 nm) of semimetal $Hg_{1-x}Cd_xTe$. In another words, the conductance due to the TPSS (or RIS) at the interfaces of the approximately 3 nm thick lower layers with the semimetal bulk part of the investigated sample with the thickness from 100 to 1280 nm, can dominate the conductance of the entire sample (see Fig. 6). That are new conceptions [2] of the electron transport in the semimetal bulk $Hg_{1-x}Cd_xTe$ that could require a reinterpretation of previous experimental results on semimetal $Hg_{1-x}Cd_xTe$ layers (with thickness less as 1300 nm) which have been obtained over the last 40 years [29–31].

Forth, in comparison with pure HgTe energy dispersion of semimetallic HgCdTe is closer to linearity in the wider range of the momentum [48] what leads to an increase in the attractiveness of the Topological Insulator based on semimetal HgCdTe alloy for future applications.

Acknowledgements

We acknowledge support from the authorities of the Podkarpackie Voivodeship (Marshals Office of the Podkarpackie Voivodeship of Poland), contract WNDPPK.01.03.00-18-053/12.

We acknowledge also E. Bobko for the performed lithography for samples investigated, as well as M. Trzyna for the SIMS measurements and Prof. W. Zawadzki, Prof. I. Izhnin, Prof. T. Wojtowicz and Prof. J. Wrobel for valuable discussions.

References

[1] P. Martyniuk, J. Antoszewski, M. Martyniuk, L. Faraone, A. Rogalski, New concepts in infrared photodetector designs, Appl. Phys. Rev. 1 (2014) 041102.
[2] G. Tomaka, J. Grendysa, P. Śliz, C.R. Becker, J. Polit, R. Wojnarowska, A. Stadler, E.M. Sheregii, High-temperature stability of electron transport in semiconductors with strong spin-orbital interaction, Phys. Rev. B 93 (2016) 205419.
[3] Shun-Qing Shen, Topological Insulators. Dirac Equation in Condensed Matter. Springer Series in Solid State Science, vol. 174, Springer, Berlin, 2013.
[4] C.L. Kane, E.J. Mele, Quantum spin Hall effect in graphene, Phys. Rev. Lett. 95 (2005) 226801–226804.
[5] B.A. Bernevig, S.-C. Zhang, Quantum spin Hall effect, Phys. Rev. Lett. 96 (2006) 106802–106804.
[6] B.A. Bernevig, T.L. Hughes, S.-C. Zhang, Quantum spin Hall effect and topological phase transition in HgTe quantum wells, Science 314 (2006) 1757–1761.
[7] M. König, S. Wiedmann, C. Brüne, A. Roth, H. Buhmann, L.W. Molenkamp, Xiao-Lian Qiand, S.-C. Zhang, Quantum spin Hall insulator state in HgTe quantum wells, Science 318 (2007) 766–770.
[8] Liang Fu, C.L. Kane, E.J. Mele, Topological insulators in three dimensions, Phys. Rev. Lett. 98 (2007) 106803–106804.
[9] Liang Fu, C.L. Kane, Topological insulators with inversion symmetry, Phys. Rev. B 76 (2007) 045302–045317.
[10] D. Hsieh, D. Qian, L. Wray, Y. Xia, Y.S. Hor, R.J. Cava, M.Z. Hasan, A topological Dirac insulator in a quantum spin Hall phase, Nature 452 (2008) 970–974.
[11] C. Brüne, C.X. Liu, E.G. Novik, E.M. Hankiewicz, H. Buhmann, Y.L. Chen, X.L. Qi, Z.X. Shen, S.-C. Zhang, L.W. Molenkamp, Quantum Hall effect from the topological surface states of strained bulk HgTe, Phys. Rev. Lett. 106 (2011) 126803–126804.
[12] A. Delin, T. Klüner, Excitation spectra and ground-state properties from density-functional theory for the inverted band-structure systems b-HgS, HgSe, and HgTe, Phys. Rev. B 66 (2002) 035117–035118.
[13] M.Z. Hasan, C.L. Kane, Topological insulators, Rev. Mod. Phys. 82 (2010) 3045–3067.
[14] Xiao-Liang Qi, Shou-Cheng Zhang, Topological insulators and superconductors, Rev. Mod. Phys. 83 (2011) 1057–1110.
[15] M. Berry, Geometric phase memories, Nat. Phys. 6 (2010) 148–150.
[16] J.E. Moore, L. Balents, Topological invariants of time-reversal-invariant band structures, Phys. Rev. B 75 (2007), 121306-4 R.
[17] Jeffrey C.Y. Teo, Liang Fu, C.L. Kane, Surface states and topological invariants in three-dimensional topological insulators: application to Bi_{1-x} Sb_x, Phys. Rev. B 78 (2008) 045426–045429.
[18] Liang Fu, C.L. Kane, Superconducting proximity effect and Majorana fermions at the surface of a topological insulator, Phys. Rev. Lett. 100 (2008), 096407-096404.
[19] I. Galanakis, P.H. Dederichs, N. Papanikolaou, Slater-Pauling behavior and origin of the half-metallicity of the full-heusler alloys, Phys. Rev. B 66 (2002), 174429–9.
[20] Wenjie Xie, Anke Weidenkaff, Xinfeng Tang, Qingjie Zhang, Joseph Poon, Terry M. Tritt, Recent advances in nanostructured thermoelectric half-heusler compounds, Nanomaterials 2 (2012) 379–412.
[21] Y. Xia, D. Qian, D. Hsieh, L. Wray, A. Pal, H. Lin, A. Bansil, D. Grauer, Y.S. Hor, R.J. Cava, M.Z. Hasan, Observation of a large-gap topological-insulator class with a single Dirac cone on the Surface, Nat. Phys. 5 (2009) 398–402.
[22] H. Zhang, C.-X. Liu, X.-L. Qi, X. Dai, Z. Fang, S.-C. Zhang, Topological insulators in Bi_2Se_3, Bi_2Te_3 and Sb_2Te_3 with a single Dirac cone on the Surface, Nat. Phys. 5 (2009) 438–442.
[23] Y.L. Chen, J.G. Analytis, J.H. Chu, Z.K. Liu, S.K. Mo, X.L. Qi, H.J. Zhang, D.H. Lu, X. Dai, Z. Fang, S.-C. Zhang, I.R. Fisher, Z. Hussain, Z.X. Shen, Experimental realization of a three-dimensional topological insulator, Bi_2Te_3, Science 325 (2009) 178–181.
[24] D.X. Qu, Y.S. Hor, J. Xiong, R.J. Cava, N.P. Ong, Quantum oscillations and hall anomaly of surface states in the topological insulator Bi2Te3, Science 329 (2010) 821–824.
[25] Tong Zhang, Jeonghoon Ha, Niv Levy, Young Kuk, Joseph Stroscio, Electric-field tuning of the surface band structure of topological insulator Sb2Te3 thin films, Phys. Rev. Lett. 111 (2013) 056803–0568035.
[26] Bahadur Singh, Ashutosh Sharma, H. Lin, M.Z. Hasan, R. Prasad, A. Bansil, Opological electronic structure and Weyl semimetal in the TlBiSe2 class of semiconductors, Phys. Rev. B 86 (2012), 115208–115207.
[27] T. Sato, Kouji Segawa, K. Kosaka, S. Souma, K. Nakayama, K. Eto, T. Minami, Yoichi Ando, T. Takahashi, Unexpected mass acquisition of Dirac fermions at the quantum phase transition of a topological insulator, Nat. Phys. 7 (2011) 840–844.
[28] Y. Xu, I. Miotkowski, C. Liu, J. Tian, H. Nam, N. Alidoust, J. Hu, C.-K. Shih, M.Z. Hasan, Y.P. Chen, Observation of topological surface state quantum Hall effect in an intrinsic three-dimensional topological insulator, Nat. Phys. 10 (2014) 956–963.
[29] R. Dornhaus, G. Nimtz, Narrow gap semiconductors Springer Tracts in Modern Physics, vol. 98, Springer, Berlin, 1983.
[30] A. Rogalski, History of infrared detectors, Opto-Electron. Rev. 20 (3) (2012) 279–308.
[31] A. Rogalski, Recent progress in infrared detector technologies, Infrared Phys. Technol. 54 (3) (2011) 136–154.
[32] D.A. Kozlov, Z.D. Kvon, E.B. Olshanetsky, N.N. Mikhailov, S.A. Dvoretsky, D. Weiss, Transport properties of a 3D topological insulator based on a strained high-mobility HgTe film, Phys. Rev. Lett. 112 (2014) 196801–196805.
[33] Z. Zang, A. Nakamura, J. Temmyo, Single cuprous oxide films synthesized by radical oxidation at low temperature for PV application, Opt. Express 21 (2013) 11448–11456.
[34] Z. Zang, A. Nakamura, J. Temmyo, Nitrogen doping in cuprous oxide films synthesized by radical oxidation at low temperature, Mater. Lett. 92 (2013) 188–191.
[35] J. Schmidt, K. Ortner, J. Jensen, C. Becker, Molecular beam epitaxially grown n type Hg0.80Cd0.20Te (112)B using iodine, J. Appl. Phys. 91 (2002) 451–455.
[36] A. Kisiel, M. Podgórny, A. Rodzik, W. Giriat, Fundamental reflection of $Cd_xHg_{1-x}Te$ crystals in the 1.9 to 3.1 eV energy range, Phys. Status Solidi B 71 (1975) 457–460.
[37] J.G. Analytis, R.D. McDonald, S.C. Riggs, J.-H. Chu, G.S. Boebinger, I.R. Fisher, Two-dimensional surface state in the quantum limit of a topological insulator, Nat. Phys. 6 (2010) 960–964.
[38] B.F. Gao, P. Gehring, M. Burghard, K. Kern, Gate-controlled linear agnetoresistance in thin BSe3 sheets, Appl. Phys. Lett. 100 (2012) 212402.
[39] J. Olea, G. Gonzalez-Daz, D. Pastor, I. Martil, A. Mart, E. Antoln, A. Luque, Two-layer Hall effect model for intermediate band Ti-implanted silicon, J. Appl. Phys. 109 (2011), 063718-8.
[40] G.M. Gusev, Z.D. Kvon, E.B. Olshanetsky, A.D. Levin, Y. Krupko, J.C. Portal, N.N. Mikhailov, S.A. Dvoretsky, Temperature dependence of the resistance of a two-dimensional topological insulator in a HgTe quantum well, Phys. Rev. B 89 (2014), 125305–5.
[41] J.S. Novoselov, A.K. Geim, S.V. Morozov, D. Jiang, M.I. Katsnelson, I.V. Grigorieva, S.V. Dubonos, A.A. Firsov, Two-dimensional gas of massless Dirac fermions in graphene, Nature 438 (2005) 197–200.
[42] Y. Zhang, Y.W. Tan, H.L. Stormer, P. Kim, Experimental observation of the quantum Hall effect and Berry's phase in graphene, Nature 438 (2005) 201–204.
[43] Yia-Chung Chang, J.N. Schulman, G. Bastard, Y. Guldner, M. Voos, Effects of quasi-interface states in HgTe-CdTe superlattices, Phys. Rev. B 31 (1985), 2557-2554.
[44] Jie Ren, Guang Bian, Li Fu, Chang Liu, Tao Wang, Gangqiang Zha, Wanqi Jie, Madhab Neupane, T. Miller, M.Z. Hasan, T.-C. Chiang, Electronic structure of the quantum spin Hall parent compound CdTe and related topological issues, Phys. Rev. B 90 (2014) 205211–205216.
[45] Christoph Brüne, Cornelius Thienel, Michael Stuiber, Jan Böttcher, Hartmut Buhmann, Elena G. Novik, Chao-Xing Liu, Ewelina M. Hankiewicz, Laurens W. Molenkamp, Dirac-screening stabilized surface-state transport in a topological insulator, Phys. Rev. X 4 (2014) 041045–041046.
[46] E.H. Hwang, S. Das Sarma, Dielectric function, screening, and plasmons in two-dimensional graphene, Phys. Rev. B 75 (2007), 205418–6.
[47] Steffen Wiedmann, Andreas Jost, Cornelius Thienel, Christoph Brüne, Philipp Leubner, Hartmut Buhmann, Laurens W. Molenkamp, J.C. Maan, Uli Zeitler, Temperature-driven transition from a semiconductor to a topological insulator, Phys. Rev. B 91 (2015) 205311–205317.
[48] M. Marchewka, Formation of Dirac point and the topological surface states inside the strained gap for mixed 3D $Hg_{1-x}Cd_xTe$, Physica E 84 (2016) 407–414.
[49] Daniel Bulmash, Chao-Xing Liu, Xiao-Liang Qi, Prediction of a weyl semimetal in Hg_{1-x-y} Cd_xMn_yTe, Phys. Rev. B 89 (2014), 081106-5(R-4).